



Highly dispersed PtPd on graphitic nanofibers and its heavy d- π effect

Yu-Xuan Xiao^a, Jie Ying^{b,c,**}, Ge Tian^a, Yong Tao^d, Hao Wei^a, Si-Yu Fan^a, Ze-Hao Sun^a,
Wan-Juan Zou^a, Jie Hu^a, Gang-Gang Chang^a, Weihua Li^b, Xiao-Yu Yang^{a,b,e,*}, Christoph Janiak^c

^a State Key Laboratory of Advanced Technology for Materials Synthesis and Processing and School of Materials Science and Engineering, Wuhan University of Technology, 122 Luoshi Road, Wuhan, 430070, China

^b School of Chemical Engineering and Technology and Southern Laboratory of Ocean Science and Engineering, Sun Yat-sen University, Zhuhai, 519082, China

^c Institut für Anorganische Chemie und Strukturchemie, Heinrich-Heine-Universität Düsseldorf, Düsseldorf, 40204, Germany

^d State Key Laboratory of Silicate Materials for Architectures, Wuhan University of Technology, 122 Luoshi Road, Wuhan, 430070, China

^e School of Engineering and Applied Sciences, Harvard University, Cambridge, Massachusetts, 02138, USA

ARTICLE INFO

Keywords:

PtPd nanoparticles
Carbon nanofibers
d- π overlap
High dispersion
Oxygen reduction reaction

ABSTRACT

The strong Pt-carbon interaction is a very promising way to high-performance design of electrocatalysts. However, the heavy d- π overlap, a high strength of Pt-C bonding, in sp² bonded graphitic carbons with low level of defects is rarely reported. Herein, PtPd nanoparticles and graphitic carbon nanofibers (PtPd/CNF) have been integrated via heavy d- π overlap by an interfacial wettability approach and their formation mechanism has also been fully elucidated. The features of strong d- π overlap and high dispersion of metals offer PtPd/CNF with enhanced ORR activity (5.8 folds of specific activity than commercial Pt/C), and excellent structural stability and electrocatalytic durability. A new “heavy d- π overlap” concept, characteristics, and mechanism are proposed at an atomic-/nanoscale to clarify the generation of the predictive interaction as well as the interface charge transfer. It is believed that the study on heavy d- π overlap sheds new light on the fundamental aspects of the nature of Pt-C interaction.

1. Introduction

The integration of Pt (Pt-alloys) and nanocarbons has been the most efficient way to enhance Pt utilization, oxygen reduction reaction (ORR) activity, and durability [1–4]. The beauty of such integration lies in the fact that nanocarbons as electrocatalyst supports have been considered to be the best choice not only due to their high electrical conductivity and high specific surface area, but also because the carbon can alter the system's Galvani potential, raise the electronic density of nanocatalysts, and lower the Fermi level, which favors the interfacial electron transfer and thus accelerates the electrode processes [5,6]. The Pt-C interaction has been therefore a very promising way to growth control and structure design of nanocatalysts, as well as their improvement of electrocatalytic activity and stability [7]. Direct deposition is the most common approach for engineering high-performance Pt-based nanocatalysts within/on nanocarbons, whatever in commercial application or fundamental research [8–10]. For example, to date, Pt-based nanoparticles on carbon black are the only practical

electrocatalysts presently used in proton exchange membrane fuel cells (PEMFCs) [11,12]. It has been found that the high surface area, accessible pore structure and rich surface defects of carbon black strongly influence the size and dispersion of Pt-based nanoparticles in electrocatalysts, affecting the number of active sites on the catalyst surface and thus influencing their ORR performance in PEMFCs [13,14]. However, the amorphous structure of carbon black often results in relatively low conductivity and electrocatalytic corrosion [15,16].

sp² bonded graphitic nanocarbons such as graphene sheets and carbon nanotubes have been expected to enhance the conductivity and stability of Pt-based electrocatalysts [17,18]. From the view of energy level point and the macroscopic surface properties, sp² bonded carbon atoms are the most thermodynamically stable form of nanocarbon [19], and thus a high strength of Pt-C bonding in graphitic carbons with low level of defects is theoretically and technologically irrational. Defect engineering [20,21], surface modifying [22,23] and heteroatom doping [8,24,25] have been chosen to decrease the thermodynamical barrier and enhance the interaction between the graphene sheet and the Pt (Pt-

* Corresponding author at: State Key Laboratory of Advanced Technology for Materials Synthesis and Processing and School of Materials Science and Engineering, Wuhan University of Technology, 122 Luoshi Road, Wuhan, 430070, China

** Corresponding author at: School of Chemical Engineering and Technology and Southern Laboratory of Ocean Science and Engineering, Sun Yat-sen University, Zhuhai, 519082, China

E-mail addresses: yingj5@mail.sysu.edu.cn (J. Ying), xyyang@whut.edu.cn (X.-Y. Yang).

<https://doi.org/10.1016/j.apcatb.2019.118080>

Received 25 February 2019; Received in revised form 14 June 2019; Accepted 11 August 2019

Available online 13 August 2019

0926-3373/ © 2019 Elsevier B.V. All rights reserved.

alloy) catalysts. All approaches share a technique core that the graphitic carbon requires to be broken for the generation of interaction between carbon and metal, however it often leads to the disadvantageous damage of atom structures, limitation of reaction kinetics and complexity of synthesis approaches. A strong Pt-C interaction therefore seems impossible in graphitic carbons with low level of defects. Recent works demonstrate that the heavy d- π overlap is a strong interaction of heavy d metals (such as Pt, Ir, and Au) with graphite [26,27], and shows the feature of partially covalent and partially ionic bonding, due to the electron delocalization between the carbon π sites and electron transfer from Pt to carbon [28]. Note that "d- π overlap" is only a predictive model to describe the strong interaction of heavy d metals (such as Pt, Ir, and Au) with graphite structure by theoretical calculation [26,27], resulting in significant change of Fermi level. As a predictive result of the heavy d- π overlap, spin-orbit splitting of the graphite π states near the Fermi level would be not only favorable to the electron transfer for enhancing the conductivity, but also lead to the improvement of the bonding strength of supported heavy d metals/carbon for stabilizing the nanometals [26]. To our best knowledge, there is no experimental verification of "d- π overlap" on Pt/carbon for activity promotion and stability enhancement in practical applications such as electrocatalysis. High-temperature treatments can lead to extension of π -sites of sp^2 hybridized carbon atoms, which can act as anchoring centers for overlapping d orbital of Pt atoms, thus increasing the strength for the Pt-C interaction [29,30]. In other words, the relatively high thermodynamic barrier caused by graphitic structure would be covered to form more and stronger d- π overlap. Therefore, the d- π overlap, as a desired strong Pt-C interaction, is theoretically possible formed between Pt and crystalline sp^2 hybridized carbon via high-temperature process. High-temperature solvothermal synthesis acts as a common approach to nanometal synthesis, and thereby provides the possibility for the formation of d- π bonding between reactive unligated metal clusters and crystalline carbon surfaces [7]. It has to be pointed out that the strong Brownian motion at high-temperature often results in random interfacial movement of metallic precursors and thus random assembling-bonding-aggregating of nanometals onto the carbon surface. Therefore, it is of scientific interest and technologic importance to create interfacial condensation of metal precursors onto a graphitic carbon surface for the generation of highly dispersed nanometals and corresponding d- π bonding.

As is well-known, the condensation from a hydrophilic reaction solution can form close packed array onto the hydrophobic smooth solid surface [31,32]. Considering that the interfacial hydrophobicity is the nature of carbon, herein, we chose the hydrophilic solvent 1,5-pentanediol and hydrophobic carbon nanofiber (CNF) as a model synthesis. Note that commercial CNF is a typical example of sp^2 hybridized graphitic nanocarbon with many unique features such as very low cost, long-rang electrical conduction, fast electron transport, and corrosion resistance [33]. Moreover, 1,5-pentanediol has three advantageous functions as following: hydrophilicity for forming close-packed array onto the hydrophobic CNFs, high-viscosity for restraining the Brownian motion of the metal precursors, and reducibility for producing the metal clusters. Highly dispersed PtPd bimetallic nanoparticles on crystalline CNFs have been synthesized, and the formation of d- π overlap could greatly enhance the activity and durability of CNF-supported PtPd nanoparticles in ORR.

2. Experimental section

2.1. Materials

Pt(acac)₂ (platinum acetylacetonate; 97%), Pd(acac)₂ (palladium acetylacetonate; 99%) 1,5-pentanediol (98%) and perchloric acid (AR, 70.0–72.0%) were purchased from Shanghai Aladdin Biochemical Polytron Technologies Inc. Polyacrylonitrile (PAN, Mw \approx 150,000) and polyvinylpyrrolidone (PVP, Mw \approx 55,000) were purchased from

Sigma-Aldrich. Ethylene glycol (EG, AR), ethanol (AR) and acetone (AR) were purchased from Sinopharm Chemical Reagent Co., Ltd. Commercial carbon nanofibers (CNFs) were purchased from Nanjing XFNANO Materials Tech Co., Ltd. Commercial Vulcan-XC 72R was purchased from Shanghai Cabot Co., Ltd. All chemical reagents were used as received without further purification. Ultrapure Milliporewater (18.2 M Ω cm) was used throughout.

2.2. Acidization of CNFs

The acidization of CNFs was according to the previous article by some modification [34]. In a typical synthesis, 5.5 g CNFs were added into a 150 mL Teflon-lined stainless steel autoclave, then 90 mL mixed acid (concentrated nitric acid and concentrated sulfuric acid with a volume ratio of 5:4) was added and kept at 150 °C for 2 h. After centrifugation and washing several times, the sample was dried and collected for further use.

2.3. Synthesis of amorphous CNFs

Amorphous CNFs were synthesized by integrating the electrospinning and carbonization processes [35]. In a typical synthesis, 1.2 g PAN was dissolved in 8.8 mL of DMF to form a homogeneous solution by vigorously stirring of the mixture for 1 h before electrospinning at a voltage of 20.0 kV. The distance between the needle and the collector was kept at 10 cm. The flow rate of the syringe was maintained at 1 mL/h. Dried at 60 °C overnight, the as-synthesized PAN nanofibers were carbonized at 800 °C for 2 h in Ar atmosphere with a heating rate of 5 °C/min.

2.4. Synthesis of PtPd/CNF

In a typical synthesis, 19.7 mg Pt(acac)₂, 15.2 mg Pd(acac)₂ and 111.1 mg PVP were added to 20 mL 1,5-pentanediol at 50 °C under stirring. Then, 50 mg commercial CNFs were added to the solution under sonication for about 30 min until it became homogeneous. After that, the mixture was heated to 215 °C under nitrogen atmosphere and reacted for 30 min in a closed reaction system and under reflux condensation. When cooling to the room temperature, the products were collected by centrifugation at 12,000 rpm for 10 min, washed with ethanol/acetone mixture for three times and dried at 60 °C for 8 h.

2.5. Synthesis of Pt/CNF, Pd/CNF, PtPd/CNF-EG, PtPd/a-CNF, PtPd/ACNF and PtPd/C

Pt/CNF and Pd/CNF were synthesized via the same synthesis procedure used in PtPd/CNF except for the absence of Pd(acac)₂ or Pt(acac)₂. PtPd/CNF-EG was synthesized via the same synthesis procedure used in PtPd/CNF except for replacing 1,5-pentanediol with ethylene glycol. PtPd/a-CNF, PtPd/ACNF and PtPd/C were synthesized via the same synthesis procedure used in PtPd/CNF except for replacing CNFs with amorphous CNFs, acidized CNFs and commercial Vulcan-XC 72R carbon, respectively.

2.6. Physical characterization

Transmission electron microscopy (TEM), high-angle annular dark-field scanning TEM (HAADF-STEM), and energy-dispersive X-ray spectroscopy (EDX) analyses were performed at 200 kV on a JEOL JEM-2100 F microscope and a FEI Talos microscope at Wuhan University of Technology. A Bruker D8 Advance X-ray diffractometer equipped with Cu K α radiation was used to obtain all the X-ray diffraction (XRD) patterns. Scanning electron microscopy (SEM) images were obtained by an S-4800 electron microscope (HITACHI). The X-ray photoelectron spectroscopy (XPS) measurements were carried out by ESCALAB 250Xi, Thermofisher, USA. Raman spectra were collected with a LabRam HR

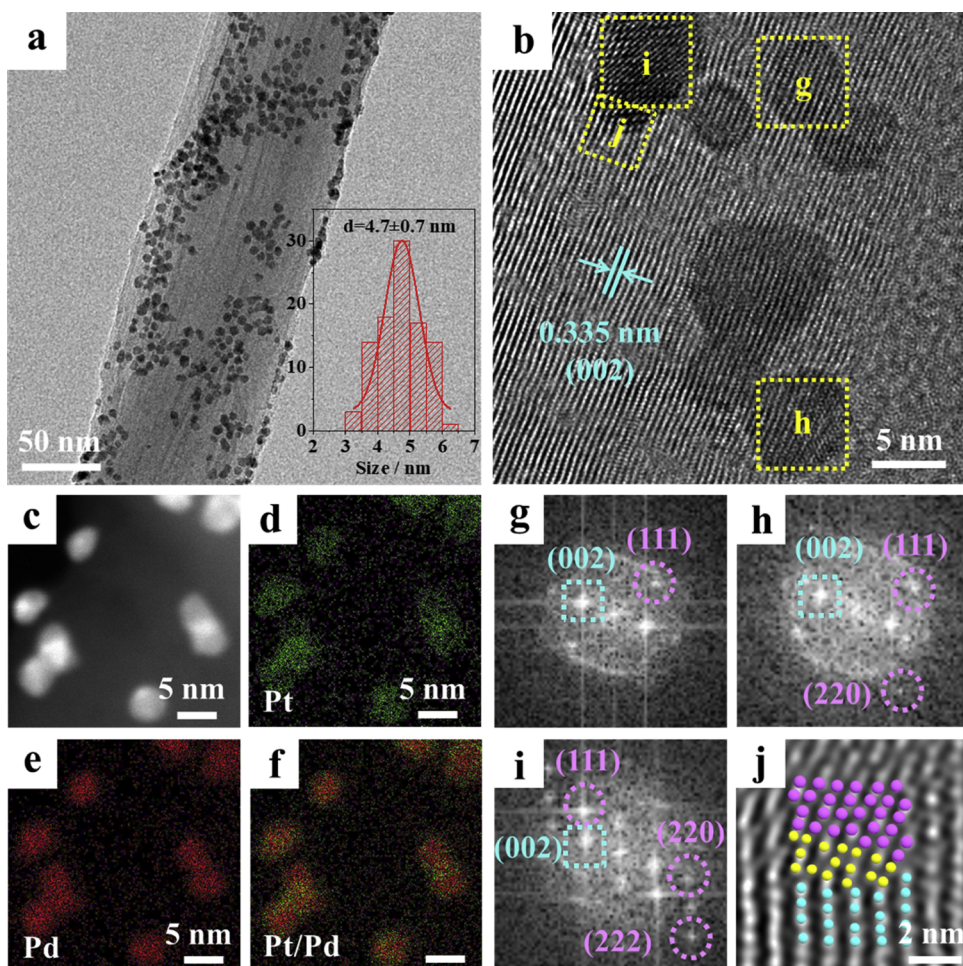


Fig. 1. (a) Representative TEM image of PtPd/CNF. Inset is the size distributions of nanocrystals. (b) High resolution TEM image of PtPd/CNF. (c) HAADF-STEM image of PtPd/CNF and (d–f) corresponding EDX elemental mapping results: (d) Pt, (e) Pd, and (f) Pt and Pd overlaid color mapping. (g–i) FFT patterns of selected areas indicated in (b), the spots marked by pink circles and blue square could be indexed to the reflection of PtPd nanocrystals and CNFs, respectively. (j) Inverse FFT of an interface between nanoparticle and carbon support in (b). The pink, blue, and yellow dots represent PtPd, CNF, and their nanofusion phase, respectively. The lattice fringe, original inverse FFT image and interpreting atomic models are given in Fig. S3 (For interpretation of the references to colour in this figure legend, the reader is referred to the web version of this article).

Evolution Raman spectrometer using an Ar^+ laser (532 nm). The functional groups of CNFs and acidized CNFs were characterized by Fourier transformation infrared spectrometer spectra (FTIR, Nexus, TherMo Nicolet, USA). An OCA35 automatic contact angle measurement device (Dephina, Germany) was used to test the contact angle of CNFs and acidized CNFs. The content analyses of different catalysts were measured by the inductively coupled plasma-atomic emission spectrometry (ICP-AES, Prodigy 7, LEEMAN LABS INC, USA). Viscosity of 1,5-pentanediol and ethylene glycol were measured on a NDJ-8S viscometer at room temperature.

2.7. Electrochemical measurements

A three-electrode cell was used for the electrochemical measurements on a Autolab working station from Metrohm, Switzerland. Typically, a Ag/AgCl (3 M) electrode was used as a reference electrode, a platinum mesh was used as a counter electrode, and a glassy-carbon Rotating Disk Electrode (RDE, diameter: 5 mm, area: 0.196 cm^2) was used as the working electrode. According to the results of ICP-AES, the loading amount of metal was $3 \mu\text{g}$. The Electrochemical Impedance Spectroscopy (EIS) tests were performed in 0.1 M HClO_4 , with the frequency range being 0.005 to $1 \times 10^5 \text{ Hz}$ and a small sine-wave distortion (AC signal) of 10 mV amplitude. The cyclic voltammetry (CV) measurements were performed in 0.1 M N_2 -saturated HClO_4 solutions at a sweep rate of 50 mV/s , and ORR measurements were carried out in 0.1 M O_2 -saturated HClO_4 solutions under O_2 flow using the glassy-carbon RDE at a rotation rate of 1600 rpm with a 10 mV/s sweep rate. The background current was measured by running the ORR in N_2 -purged 0.1 M HClO_4 to account for capacitive current contributions.

This background current was subtracted from the experimental ORR current to eliminate any capacitive current contributions [36,37]. The accelerated durability tests (ADTs) were performed in 0.1 M HClO_4 solution under air conditions with cyclic potential sweeps between 0.6 and 1.1 V versus reversible hydrogen electrode (RHE) at a 50 mV/s sweep rate for 8000 cycles. All potentials were converted to values with reference to RHE.

2.8. Density functional theory (DFT) calculations

To simulate the composite configuration of PtPd nanoparticles on graphite CNF, we construct a $6 \times 6 \times 1$ slab of graphite crystal containing 144 carbon atoms, with a vacuum thickness of 25 \AA . A PtPd cluster with equivalent Pt and Pd sites is constructed and finely pre-optimized by structural relaxation before applied on the graphite surface. The upper graphite layer close to the PtPd cluster is free to relax while the underlying layer is constrained as the stable bulk matrix. The electronic property calculation is performed after a full structural relaxation of the composite model, and the geometry optimization was based on the energy minimization method. The Cambridge Sequential Total Energy Package (CASTEP) [38] is employed for the DFT calculation. The exchange-correlation potential is disposed by Perdew-Burke-Ernzerhof (PBE) within the framework of generalized gradient approximation (GGA) [39]. The kinetic energy cutoff is 540 eV and integration of the first Brillouin zone is performed at the gamma point. The convergence tolerances of the total energy and residual force are 10^{-6} eV and 0.01 eV/\AA per atom, respectively.

3. Results and discussion

The highly dispersed PtPd bimetallic nanoparticles on crystalline CNFs (denoted as PtPd/CNF) were synthesized through an interfacial wettability approach in the solvent of 1,5-pentanediol with polyvinylpyrrolidone (PVP) as the surfactant in the presence of commercial CNFs at high temperature (215 °C). The as-synthesized products were initially measured by XRD. As shown in Fig. S1, the sharp peak at 26.4° represents the (002) plane of graphite (ICDD no. 41-1487) in CNFs [40,41] and the other four peaks at 40.1°, 46.6°, 68.0°, and 82.0° can be readily indexed to the (111), (200), (220), and (311) reflections of face-centered cubic (fcc) PtPd (ICDD no. 65-6418), which are in agreement with those of the previous reports [42,43]. Meanwhile, as determined by ICP-AES measurement, the molar ratio between Pt and Pd in PtPd/CNF is around 1:1, which coincides with the Pt/Pd atomic ratio in the initial reaction, revealing that the Pt and Pd precursors are completely reduced in the synthesis.

Fig. 1a shows the representative TEM image of PtPd/CNF. As can be seen, plenty of nanoparticles with an average size of 4.7 nm are highly dispersed on the CNF support. Fig. 1b shows the high-resolution TEM image of PtPd/CNF, where the lattice fringes of both CNF and nanoparticles can be clearly seen, indicating their high crystalline structure. The lattice fringes with interplanar spacing of 0.335 nm are consistent with the (002) plane of graphitic CNF. Notably, the lattice fringes of these nanoparticles are well merged with lattice fringes of the crystalline carbon support, suggesting their highly integrated nanostructure. Fig. 1c-f and Fig. S2 show HAADF-STEM images of PtPd/CNF and the corresponding EDX mapping results. Pt elements are distributed on the outer surface of these nanoparticles while Pd elements are all lied on the center of these nanoparticles, demonstrating a typical core-shell nanostructure with a Pt-skin, which can be possibly attributed to the different standard reduction potential of Pt(II)/Pt and Pd(II)/Pd, and the preferential interaction of Pt-C. Fig. 1g-i show the Fast Fourier Transform (FFT) patterns of three areas of PtPd nanoparticles on CNF indicated in Fig. 1b. Two sets of spots belong to different crystalline structures and can be identified in all these patterns. One originated from the (002) plane of graphitic CNF (square), and the other is indexed to the (111), (200), or (222) planes of PtPd (circle), indicating that various planes of PtPd can be merged with crystalline CNF. This can be potentially ascribed to the high-temperature synthesis condition, which can effectively decrease the relatively high thermodynamic barrier in crystalline carbon, making it possible to merge and/or bond with the different planes of PtPd nanoparticles. To further indicate these interfacial merging, an inverse FFT of the interface between metal and carbon (Fig. 1j and Fig. S3) was investigated, and a nanofusion layer with disordered configuration (yellow dots) can be clearly seen between the ordered arrangements of PtPd (pink dots) and CNF (blue dots). In view of the Pt-skin nanostructure, the formation of interfacial nanofusion phase is probably due to Pt-C interaction.

To further confirm the Pt-C interaction between catalyst and support in our synthesis, XPS measurement was exploited. PtPd nanoparticles supported on amorphous CNFs derived from electrospinning of polyacrylonitrile and commercial Vulcan carbon with amorphous spherical structure (denoted as PtPd/a-CNF and PtPd/C, respectively; see Figs. S4 and S5 for their structure measurements) were prepared for comparison. Pt and Pd nanoparticles supported on graphitic CNFs were also fabricated as references. As shown in Fig. 2a, the Pt 4f core level for PtPd/CNF and Pt/CNF have an obviously positive shift with ~ 0.2 eV relative to PtPd/a-CNF, PtPd/C and commercial Pt/C, which is attributed to the decrease of the electron-electron repulsion in the Pt atoms, due to the charge transfer from Pt to the graphite carbon nanofibers [44]. Such a positive shift is not seen for amorphous carbon or Vulcan carbon supports. This result supports the formation of Pt-C interaction in PtPd/CNF and Pt/CNF. Moreover, the XPS data clearly demonstrates that there are mainly Pt⁰ with small portion of Pt²⁺ on the surface (Fig. S6). The relative intensity of metallic Pt⁰ for PtPd/CNF, Pt/CNF, PtPd/

a-CNF PtPd/C and commercial Pt/C was calculated to be 86.6%, 82.8%, 77.1%, 72.9% and 77.3%. The higher content of Pt⁰ in PtPd/CNF reflects the higher corrosion resistance of Pt, and thus better electrochemical stability [45]. Meanwhile, PtPd/CNF, Pd/CNF, PtPd/a-CNF and PtPd/C show very close binding energies in the Pd 3d core level (Fig. S7). Moreover, DFT calculations were conducted to further verify the Pt-C interaction. Fig. 2b and Fig. S8 show the calculated electron cloud structures of the PtPd nanoparticle supported on the surface of graphite CNF. The upper layer as the graphite surface wrinkles to form an obvious interaction with the PtPd cluster as presented by the overlap of the d electron clouds of metals and π electron clouds of carbons. In contrast, the underlying carbon layer representing the graphite bulk matrix arranges to form a flat plane enveloped by homogeneous electron density known as π electrons, which indicates no interaction with the distant PtPd nanoparticle. To further understand the bonding structures of Pt, Pd and C atoms, the electron density difference (EDD) was calculated (Fig. 2c). The EDD visualizes the electron transfer behaviors between atoms with interaction. The blue and red isosurfaces in Fig. 2c represent electron depletion and accumulation, respectively. The electron decomposition on the Pt atom is much conspicuous than that on the Pd atom as depicted by enhanced blue color, which indicates a stronger polarization and bonding effect with carbon atoms [46]. Moreover, the petal-like shape of Pt electron cloud changes greatly and a stretched electron cloud can be observed in accumulation isosurfaces of the corresponding carbon atom (top in Fig. 2c), suggesting the formation of d- π overlap. The petal-like electron cloud of Pd 4d remains intact (down in Fig. 2c), and further confirms the very weak interaction between the Pd and C atoms, which is in good agreement with the Pt-skin structure in TEM observation and almost no shift of Pd 3d core level in XPS data. The partial density of states (PDOS) in Fig. 2d provides more details of the overlap of Pt, Pd, and C atom. The PDOS of Pt 5d and C 2p show an apparent resonance near Fermi level, indicating an evident bonding effect [47]. As for Pd 4d orbitals, the resonance with C 2p is not as obvious as Pt atoms, implying a relatively weak bonding with carbon atoms, and this result is in accordance with the EDD results (Fig. 2c). In addition, the calculated distance of Pt-C in PtPd/CNF is 2.21 Å, which is close to the reported value of 2.20 Å for Pt-C interaction, supporting the mixing of covalent and ionic nature of d- π overlap [48]. The accordance of XPS result and DFT calculation supports the existence of d- π overlap in PtPd/CNF. Due to the relatively higher graphitic content in crystalline carbon, the Pt- π orbital bonding strength will be enhanced [24], and form the partially ionic and partially covalent d- π overlap. The ionic nature of d- π overlap will lower the Fermi level, which favors the electron transfer at the electrode-electrolyte interface and thus accelerate the electrode processes [49,50]. Moreover, the partially covalent bond enables to stabilize the nanoparticles on carbon, preventing them from dissolution or oxidation in the long-term catalysis, and thus could enhance the durability of catalysts [51]. The benefit of this interaction can be witnessed from the EIS tests. After supporting PtPd nanoparticles, the electrical conductivity of PtPd/CNF shows significant improvement, while PtPd/a-CNF and PtPd/C show slight changes in their electrical conductivity (Fig. S9), ascribing the former to the existence of d- π overlap, which further supports that d- π bonding to crystalline CNF is stronger than the interaction between Pt and amorphous carbon. Such a stronger overlap could greatly change the interfacial electron density, and thus accelerate the electrode processes.

The formation mechanism of integration of highly dispersed PtPd and crystalline CNFs and corresponding d- π overlap is proposed in Fig. 3. After mixing the metal precursors, carbon, PVP and 1,5-pentanediol (Fig. 3a, b), the condensed droplets may form a close-packing by self-assembly because of the wetting properties of the carbon surface [31,52]. During high-temperature synthesis, the high-viscosity of 1,5-pentanediol restrains the Brownian motion of interfacial condensation and maintains the droplets onto the CNF surface. At the same time, the nanoclusters of PtPd form and grow onto the carbon surface (Fig. 3c),

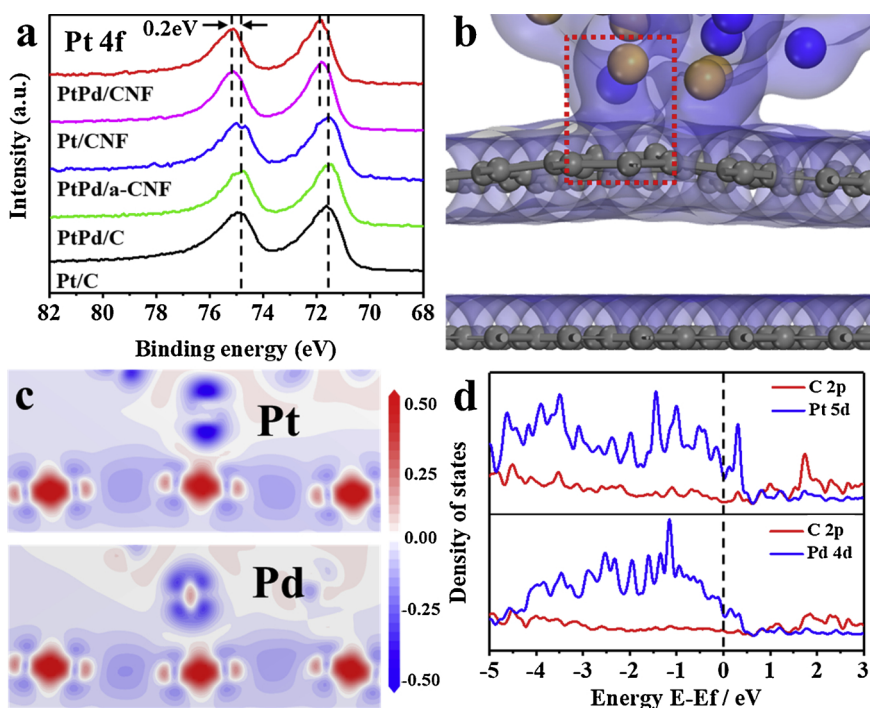


Fig. 2. (a) XPS spectra showing the binding energy of Pt 4f signals. (b) Calculated electron cloud structures of the PtPd nanoparticle supported on the surface of graphite CNF, the yellow, blue, and gray spheres represent Pt, Pd, and carbon atoms, respectively. The full image of calculated electron cloud structures of PtPd/CNF are given in Fig. S7. (c) EDD of Pt, Pd, and carbon atoms in selected area of (b), the blue and red isosurfaces represent electron depletion and accumulation, respectively. (d) PDOS of Pt, Pd, and C atoms in plot (c) (For interpretation of the references to colour in this figure legend, the reader is referred to the web version of this article).

while the high thermodynamic barrier of crystalline carbon would be decreased in order to start the formation of d- π overlap. Notably, the high temperature process can provide more potential to enhance defects on CNFs. As shown in Fig. S10, the integral intensity ratio of G band (1580 cm^{-1}) and D band (1340 cm^{-1}) (I_G/I_D , calculated by Raman spectra) for PtPd/CNF is calculated as 3.27, which has a decrease compared to the value of 4.08 for initial CNF. The lower I_G/I_D demonstrates more unsaturated and/or disordered structures in PtPd/CNF [53], which could be attributed to the formation of overlaps between the heavy d clouds of Pt and big π clouds of carbon and

irreversible disorders of sp^2 bonded carbon atoms. In contrast, the I_G/I_D ratio of PtPd/a-CNF (0.47) shows little change compared to initial amorphous CNF (0.48), which is probably due to the weak interaction of PtPd and amorphous CNF. With prolongation of time, small contact area between the hydrophobic surface and hydrophilic solvent would limit the growth of the nanometals and Brownian motion, and enhance the d- π overlap, leading to high dispersion and strong interaction of the nanometals (Fig. 3d, e). Finally, PtPd bimetallic nanoparticles highly disperse on crystalline CNFs (Fig. 3f), and the d- π overlap is formed (Fig. 3g, h). For comparison, 1,5-pentanediol (110.0 mPa·s; Table S1)

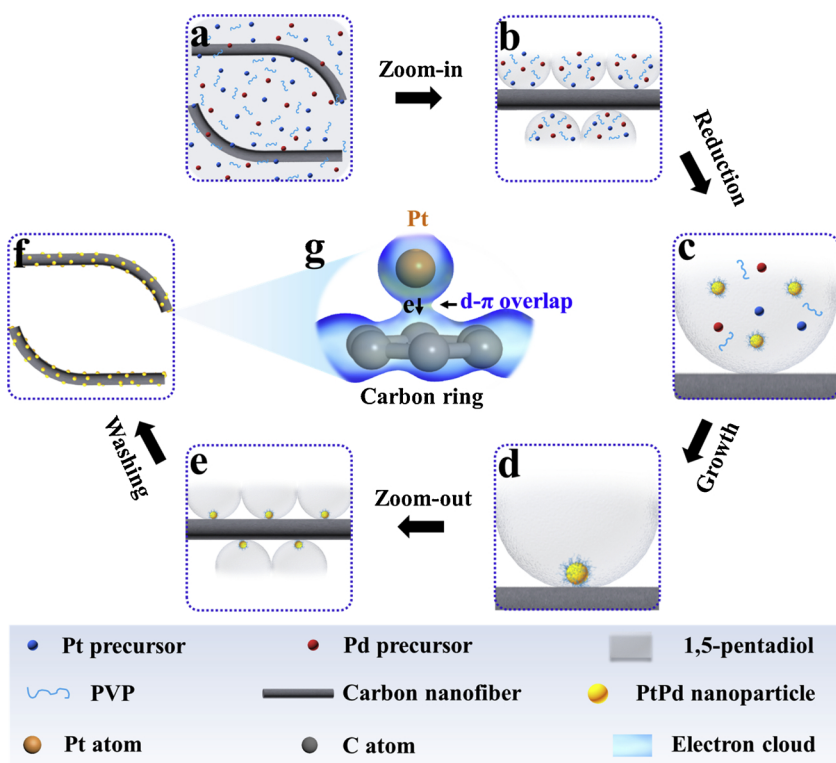


Fig. 3. Scheme illustration of the proposed formation mechanism of highly dispersed metal nanoparticles in PtPd/CNF and its d- π overlap. (a) Homogeneously dispersed Pt precursors, Pd precursors, PVP and CNFs in 1,5-pentanediol. (b) Close packed array of pentanediol on the hydrophobic CNFs. (c) Formation of PtPd crystal seeds at high temperature. (d) Limited growth of PtPd nanocrystals on the small contact area. (e) Homogeneous dispersion of PtPd nanocrystals on CNF. (f) Finally products after washing. (g) d- π overlap of Pt with C atoms.

was replaced by a low viscosity solvent of ethylene glycol (19.6 mPa s; Table S1) while keeping the other synthesis conditions same to prepare PtPd nanoparticles (denoted as PtPd/CNF-EG). Obviously aggregated nanoparticles on CNF are observed in PtPd/CNF-EG (Fig. S11a), which can be ascribed to the relatively fast diffusion and mobility of metal precursors/nanoclusters due to the faster Brownian motion in the lower viscosity solvent. To investigate the influence of interfacial wettability on the dispersion of metal nanoparticles, CNFs were acidized for changing their hydrophilic/hydrophobic property. After acidization, the morphology and crystalline structure of CNFs show no change (Fig. S12 and Fig. S13), while CNFs were converted to be hydrophilic, as confirmed by the contact angle result (Fig. S14) because of the introduction of the hydrophilic groups of $-C-O$, $-C=O$, $-OH$ (Fig. S15). For comparison, PtPd nanoparticles on acidized CNFs (denoted as PtPd/ACNF) were prepared under the same synthesis conditions but replacing CNFs with hydrophilic acidized CNFs. As shown in Fig. S11b, serious aggregation of nanoparticles is found in PtPd/ACNF, which can be attributed to the fast deposition speed of nanoparticles onto acidized CNFs due to the high interfacial wettability and large contact area between the hydrophilic reaction solution and the hydrophilic support. Overall, our results indicate that highly dispersed metal nanoparticles with strong d- π overlap can be effectively synthesized by an interfacial wettability approach in high-temperature and high-viscosity conditions.

To examine the ORR activity of PtPd/CNF, CV and linear sweep voltammetry (LSV) were carried out. PtPd/a-CNF, PtPd/CNF-EG, PtPd/ACNF, and commercial Pt/C catalysts were also evaluated under the same conditions as references. Fig. 4a shows CV curves of all these catalysts conducted in N_2 -purged 0.1 M $HClO_4$ solution with a sweep rate of 50 mV/s at room temperature. The electrochemical active surface area (ECSA) was obtained by measuring the charge collected in the hydrogen adsorption/desorption region after correction of the double-layer formation and supposing an adsorption value of 0.21 mC/cm^2 for a hydrogen monolayer. Based on the Pt mass, the ECSAs of PtPd/CNF, PtPd/a-CNF, PtPd/CNF-EG, PtPd/ACNF, and commercial Pt/C are $44.7 \text{ m}^2/\text{g}$, $41.5 \text{ m}^2/\text{g}$, $34.4 \text{ m}^2/\text{g}$, $25.2 \text{ m}^2/\text{g}$, and $69.2 \text{ m}^2/\text{g}$, respectively. Fig. 4b shows ORR polarization curves of these catalysts conducted in O_2 -saturated 0.1 M $HClO_4$ solution with a sweep rate of 10 mV/s at room temperature. In accordance with the Koutecky-Levich

equation [54], the kinetic current density was calculated and then normalized to the Pt amount and ECSA for obtaining the mass activity and specific activity, respectively (Table S3). Fig. 4c and Fig. S16 displays the mass activities of these catalysts at 0.9 V vs RHE. PtPd/CNF exhibits a remarkable mass activity of $0.420 \text{ mA}/\mu\text{g}_{Pt}$, which is about 1.6, 4.5, 9.1, and 3.7 times higher than that of PtPd/a-CNF ($0.268 \text{ mA}/\mu\text{g}_{Pt}$), PtPd/CNF-EG ($0.093 \text{ mA}/\mu\text{g}_{Pt}$), PtPd/ACNF ($0.046 \text{ mA}/\mu\text{g}_{Pt}$), and commercial Pt/C ($0.113 \text{ mA}/\mu\text{g}_{Pt}$), respectively. Moreover, the specific activity of PtPd/CNF ($0.940 \text{ mA}/\text{cm}^2$) is about 1.5, 3.5, 5.1, and 5.8 times higher than that of PtPd/a-CNF ($0.646 \text{ mA}/\text{cm}^2$), PtPd/CNF-EG ($0.270 \text{ mA}/\text{cm}^2$), PtPd/ACNF ($0.183 \text{ mA}/\text{cm}^2$), and commercial Pt/C ($0.163 \text{ mA}/\text{cm}^2$), respectively (Fig. 4d). Notably, both the mass activity and specific activity of PtPd/CNF are higher than that of the previously reported carbon supported Pt-based catalysts (Table S4). These results demonstrate that PtPd/CNF possesses superior ORR activity compared to PtPd/CNF-EG, PtPd/ACNF, and commercial Pt/C, which can be ascribed to the strong d- π overlap and synergistic effect of the two metallic components.

The ADTs were also performed to evaluate the stability of PtPd/CNF and commercial Pt/C by performing 8000 potential cycles between 0.6 and 1.1 V vs RHE in 0.1 M $HClO_4$ solution with a sweep rate of 50 mV/s at room temperature. With increasing CV cycle numbers, PtPd/CNF displays a slight drop for the values of current densities in the hydrogen adsorption-desorption regions of 0-0.37 V vs RHE (Fig. 5a). In contrast, the values of current densities in the same regions for commercial Pt/C exhibit conspicuous drops (Fig. 5b). PtPd/CNF exhibits a loss of only 25.1% in ECSA after 8000 potential cycles, whereas the ECSA of commercial Pt/C show dramatic losses of 52.3% (Fig. S17). The result demonstrates that the electrochemical durability of PtPd/CNF is also far better than that of commercial Pt/C. Fig. 5c,d show the polarization curves of these catalysts before and after ADT. After 8000 potential cycles, PtPd/CNF show a loss of 28 mV in half-wave potential, which is much lower than that of commercial Pt/C (74 mV in half-wave potential). After 4000 and 8000 cycles, PtPd/CNF exhibits mass activities of $0.315 \text{ mA}/\mu\text{g}_{Pt}$ and $0.260 \text{ mA}/\mu\text{g}_{Pt}$, which are 4.9 and 8.4 folds of commercial Pt/C ($0.064 \text{ mA}/\mu\text{g}_{Pt}$ and $0.031 \text{ mA}/\mu\text{g}_{Pt}$), respectively (Fig. 5e). Meanwhile, the specific activities of PtPd/CNF are $0.784 \text{ mA}/\text{cm}^2$ and $0.776 \text{ mA}/\text{cm}^2$, which are 5.7 and 8.3 folds of commercial Pt/C ($0.137 \text{ mA}/\text{cm}^2$ and $0.093 \text{ mA}/\text{cm}^2$) after 4000 and 8000

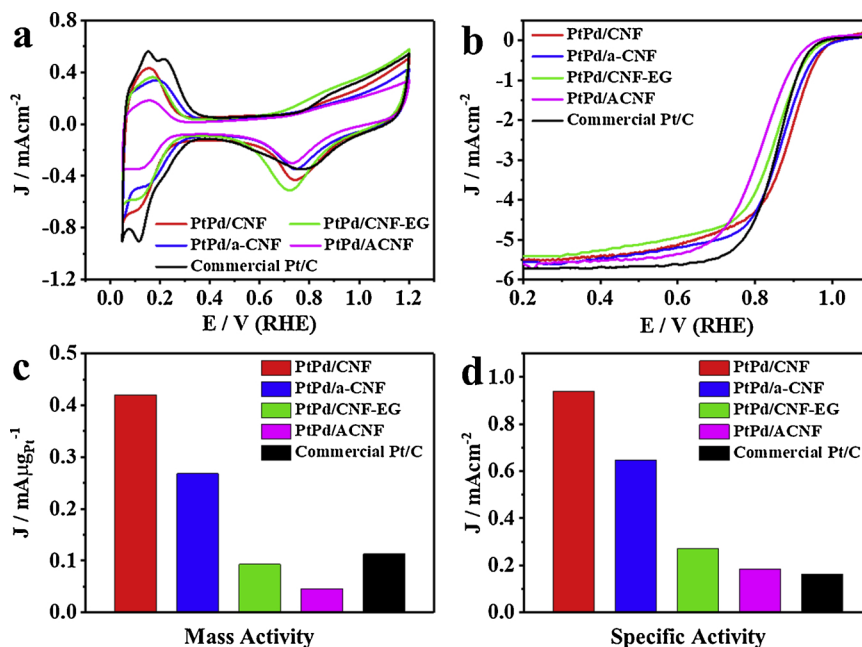


Fig. 4. (a) CV curves, (b) ORR polarization curves, (c) mass activity and (d) specific activity at 0.9 V vs RHE of PtPd/CNF, PtPd/a-CNF, PtPd/CNF-EG, PtPd/ACNF, and commercial Pt/C.

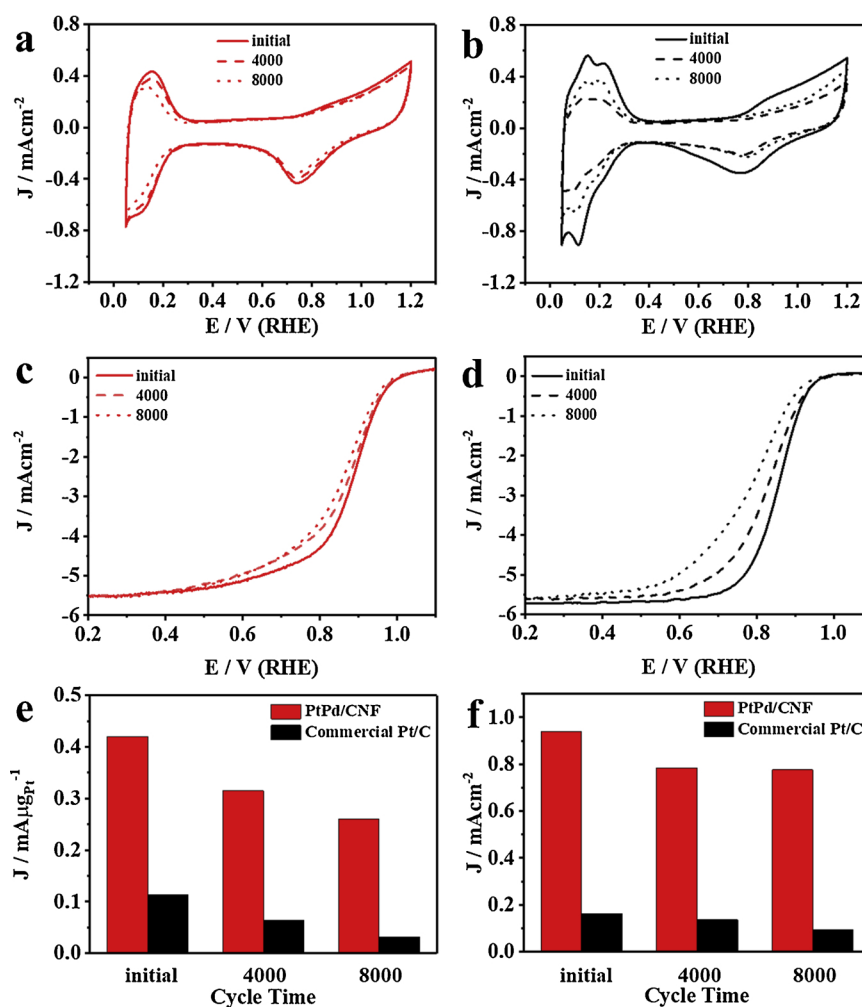


Fig. 5. CV curves of (a) PtPd/CNF and (b) commercial Pt/C after different potential sweep cycles. ORR polarization curves of (c) PtPd/CNF and (d) commercial Pt/C after different potential sweep cycles. (e) Mass activity and (f) specific activity at 0.9 V vs RHE of PtPd/CNF and commercial Pt/C after different potential sweep cycles.

potential cycles, respectively (Fig. 5f). Notably, after 8000 potential cycles, the size and dispersity of nanoparticles in PtPd/CNF show no distinct change (Fig. S18), while the originally dispersed commercial Pt/C (Fig. S19a) turned into heavy aggregation (Fig. S19b). Therefore, PtPd/CNF with high dispersion and strong d- π overlap has demonstrated a greatly improved ORR activity and durability.

4. Conclusions

In summary, we have presented a simple interface-wettability method to synthesize highly dispersed PtPd nanoparticles integrated with commercial CNFs via d- π overlap. The existence of d- π overlap has been revealed by both experiment results and DFT calculations. Moreover, the formation mechanism of integration of PtPd and crystalline CNFs has been fully illustrated, and its d- π overlap effect results in efficient catalytic activity and extraordinary durability in ORR. The synthesis method described herein indeed holds great potential in the low-cost approach to synthesize nanocarbon-supported nanocatalysts with outstanding performance for practical applications and also create a fundamental aspect of the nature of Pt-C interaction.

Declaration of Competing Interest

The authors declare that they have no known competing financial interests or personal relationships that could have appeared to

influence the work reported in this paper.

Acknowledgements

This work was supported by NSFC (51861135313, 51472190, 51503166, 51611530672, 21711530705), ISTCP (2015DFE52870), HPNSF (2016CFA033, 2017CFB487), and Jilin Province Science and Technology Development Plan 20180101208JC.

Appendix A. Supplementary data

Supplementary material related to this article can be found, in the online version, at doi:<https://doi.org/10.1016/j.apcatb.2019.118080>.

References

- [1] M. Zhou, H.-L. Wang, S.-J. Guo, Towards high-efficiency nanoelectrocatalysts for oxygen reduction through engineering advanced carbon nanomaterials, *Chem. Soc. Rev.* 45 (2016) 1273–1307.
- [2] Z.-F. Li, L. Xin, F. Yang, Y. Liu, Y. Liu, H. Zhang, L. Stanciu, J. Xie, Hierarchical polybenzimidazole-grafted graphene hybrids as supports for Pt nanoparticle catalysts with excellent PEMFC performance, *Nano Energy* 16 (2015) 281–292.
- [3] J. Ying, G. Jiang, Z.P. Cano, L. Han, X.-Y. Yang, Z. Chen, Nitrogen-doped hollow porous carbon polyhedrons embedded with highly dispersed Pt nanoparticles as a highly efficient and stable hydrogen evolution electrocatalyst, *Nano Energy* 40 (2017) 88–94.
- [4] J. Ying, J. Li, G. Jiang, Z.P. Cano, Z. Ma, C. Zhong, D. Su, Z. Chen, Metal-organic frameworks derived platinum-cobalt bimetallic nanoparticles in nitrogen-doped

- hollow porous carbon capsules as a highly active and durable catalyst for oxygen reduction reaction, *Appl. Catal. B: Environ.* 225 (2018) 496–503.
- [5] X. Yu, S. Ye, Recent advances in activity and durability enhancement of Pt/C catalytic cathode in PEMFC Part I. Physico-chemical and electronic interaction between Pt and carbon support, and activity enhancement of Pt/C catalyst, *J. Power Sources* 172 (2007) 133–144.
- [6] I.V. Zenyuk, S. Litster, Spatially resolved modeling of electric double layers and surface chemistry for the hydrogen oxidation reaction in water-filled platinum-carbon electrodes, *J. Phys. Chem. C* 116 (2012) 9862–9875.
- [7] Y.J. Wang, N. Zhao, B. Fang, H. Li, X.T. Bi, H. Wang, Carbon-supported Pt-based alloy electrocatalysts for the oxygen reduction reaction in polymer electrolyte membrane fuel cells: particle size, shape, and composition manipulation and their impact to activity, *Chem. Rev.* 115 (2015) 3433–3467.
- [8] D. Marquardt, F. Beckert, F. Pennetret, F. Tölle, R. Mülhaupt, O. Riant, S. Hermans, J. Barthel, C. Janiak, Hybrid materials of platinum nanoparticles and thiol-functionalized graphene derivatives, *Carbon* 66 (2014) 285–294.
- [9] Y. Huang, Y.E. Miao, S. Ji, W.W. Tjiu, T. Liu, Electrospun carbon nanofibers decorated with Ag-Pt bimetallic nanoparticles for selective detection of dopamine, *ACS Appl. Mater. Inter.* 6 (2014) 12449–12456.
- [10] A. Aboagye, H. Elbohy, A.D. Kelkar, Q. Qiao, J. Zai, X. Qian, L. Zhang, Electrospun carbon nanofibers with surface-attached platinum nanoparticles as cost-effective and efficient counter electrode for dye-sensitized solar cells, *Nano Energy* 11 (2015) 550–556.
- [11] D.S. He, D. He, J. Wang, Y. Lin, P. Yin, X. Hong, Y. Wu, Y. Li, Ultrathin icosahedral Pt-enriched nanocage with excellent oxygen reduction reaction activity, *J. Am. Chem. Soc.* 138 (2016) 1494–1497.
- [12] Jong Yoo, S.K. Kim, T.Y. Jeon, S. Jun Hwang, J.G. Lee, S.C. Lee, K.S. Lee, Y.H. Cho, Y.E. Sung, T.H. Lim, Enhanced stability and activity of Pt-Y alloy catalysts for electrocatalytic oxygen reduction, *Chem. Commun.* 47 (2011) 11414–11416.
- [13] Y.-J. Wang, D.P. Wilkinson, J. Zhang, Noncarbon support materials for polymer electrolyte membrane fuel cell electrocatalysts, *Chem. Rev.* 111 (2011) 7625–7651.
- [14] B. Fang, M. Kim, J. Kim, M. Song, Y. Wang, H. Wang, D. Wilkinson, J.J. Yu, High Pt loading on functionalized multiwall carbon nanotubes as a highly efficient cathode electrocatalyst for proton exchange membrane fuel cells, *J. Mater. Chem.* 21 (2011) 8066–8073.
- [15] S.M. Andersen, M. Borghei, P. Lund, Y.-R. Elina, A. Pasanend, E. Kauppinen, V. Ruiz, P. Kauranen, E.M. Skou, Durability of carbon nanofiber (CNF) & carbon nanotube (CNT) as catalyst support for Proton Exchange Membrane Fuel Cells, *Solid State Ion.* 231 (2013) 94–101.
- [16] D.A. Stevens, M.T. Hicksc, G.M. Haugenc, J.R. Dahnc, Ex situ and in situ stability studies of PEMFC catalysts effect of carbon type and humidification on degradation of the carbon, *J. Electrochem. Soc.* 152 (2005) A2309–A2315.
- [17] J. Zhu, M. Xiao, X. Zhao, C. Liu, J. Ge, W. Xing, Strongly coupled Pt nanotubes/N-doped graphene as highly active and durable electrocatalysts for oxygen reduction reaction, *Nano Energy* 13 (2015) 318–326.
- [18] A.O. Al-Youbi, J.L. Gómez de la Fuente, F.J. Pérez-Alonso, A.Y. Obaid, J.L.G. Fierro, M.A. Peña, M.A. Salam, S. Rojas, Effects of multiwalled carbon nanotube morphology on the synthesis and electrocatalytic performance of Pt supported by multiwalled carbon nanotubes, *Appl. Catal. B: Environ.* 150–151 (2014) 21–29.
- [19] D. Jariwala, V.K. Sangwan, L.J. Lauhon, T.J. Marks, M.C. Hersam, Carbon nanomaterials for electronics, optoelectronics, photovoltaics, and sensing, *Chem. Soc. Rev.* 42 (2013) 2824–2860.
- [20] T. Maiyalagan, Silicotungstic acid stabilized Pt–Ru nanoparticles supported on carbon nanofibers electrodes for methanol oxidation, *Int. J. Hydrogen Energ.* 34 (2009) 2874–2879.
- [21] J. Guo, G. Sun, Q. Wang, G. Wang, Z. Zhou, S. Tang, L. Jiang, B. Zhou, Q. Xin, Carbon nanofibers supported Pt–Ru electrocatalysts for direct methanol fuel cells, *Carbon* 44 (2006) 152–157.
- [22] D. He, C. Zeng, C. Xu, N. Cheng, H. Li, S. Mu, M. Pan, Polyaniline-functionalized carbon nanotube supported platinum catalysts, *Langmuir* 27 (2011) 5582–5588.
- [23] R.-X. Wang, Y.-J. Fan, L. Wang, L.-N. Wu, S.-N. Sun, S.-G. Sun, Pt nanocatalysts on a polyindole-functionalized carbon nanotube composite with high performance for methanol electrooxidation, *J. Power Sources* 287 (2015) 341–348.
- [24] D. Higgins, M.A. Hoque, M.H. Seo, R. Wang, F. Hassan, J.-Y. Choi, M. Pritzker, A. Yu, J. Zhang, Z. Chen, Development and simulation of sulfur-doped graphene supported platinum with exemplary stability and activity towards oxygen reduction, *Adv. Funct. Mater.* 24 (2014) 4325–4336.
- [25] Y. Zhou, K. Neyerlin, T.S. Olson, S. Pylypenko, J. Bult, H.N. Dinh, T. Gennett, Z. Shao, R. O’Hayre, Enhancement of Pt and Pt-alloy fuel cell catalyst activity and durability via nitrogen-modified carbon supports, *Energy Environ. Sci.* 3 (2010) 1437–1446.
- [26] I.I. Klimovskikh, S.S. Tsirkin, A.G. Rybkin, A.A. Rybkina, M.V. Filianina, E.V. Zhizhin, E.V. Chulkov, A.M. Shikin, Nontrivial spin structure of graphene on Pt (111) at the Fermi level due to spin-dependent hybridization, *Phys. Rev. B* 90 (2014) 235431.
- [27] A.M. Shikin, A.A. Rybkina, A.G. Rybkin, I.I. Klimovskikh, P.N. Skirdkov, K.A. Zvezdin, A.K. Zvezdin, Spin current formation at the graphene/Pt interface for magnetization manipulation in magnetic nanodots, *Appl. Phys. Lett.* 105 (2014) 042407.
- [28] G. Gupta, D.A. Slanac, P. Kumar, J.D. Wiggins-Camacho, J. Kim, R. Ryoo, K.J. Stevenson, K.P. Johnston, Highly stable Pt/ordered graphitic mesoporous carbon electrocatalysts for oxygen reduction, *J. Phys. Chem. C* 114 (2010) 10796–10805.
- [29] Y. Xin, J.-G. Liu, Y. Zhou, W. Liu, J. Gao, Y. Xie, Y. Yin, Z. Zou, Preparation and characterization of Pt supported on graphene with enhanced electrocatalytic activity in fuel cell, *J. Power Sources* 196 (3) (2011) 1012–1018.
- [30] M. Liu, R. Zhang, W. Chen, Graphene-supported nanoelectrocatalysts for fuel cells: synthesis, properties, and applications, *Chem. Rev.* 114 (2014) 5117–5160.
- [31] B.-L. Su, C. Sanchez, X.-Y. Yang, Hierarchically Structured Porous Materials: From Nanoscience to Catalysis, Separation, Optics, Energy, and Life Science, Wiley-VCH, Weinheim, Germany, 2012.
- [32] M. Srinivasarao, D. Collings, A. Philips, S. Patel, Three-dimensionally ordered array of air bubbles in a polymer film, *Science* 292 (2001) 79–83.
- [33] E. Antolini, Carbon supports for low-temperature fuel cell catalysts, *Appl. Catal. B: Environ.* 88 (2009) 1–24.
- [34] L. Li, J. Meng, C. Hou, Q. Zhang, Y. Li, Hao Yu, H. Wang, Dual-mechanism and multimotion soft actuators based on commercial plastic film, *ACS Appl. Mater. Interfaces* 10 (2018) 15122–15128.
- [35] T.T. Yang, H. Zhu, M. Wan, L. Dong, M. Zhang, M.L. Du, Highly efficient and durable PtCo alloy nanoparticles encapsulated in carbon nanofibers for electrochemical hydrogen generation, *Chem. Commun.* 52 (2016) 990–993.
- [36] Y. Garsany, I.L. Singer, K.E. Swider-Lyons, Impact of film drying procedures on RDE characterization of Pt/VC electrocatalysts, *J. Electroanal. Chem.* 662 (2011) 396–406.
- [37] M. Sereydych, K.L. szlu, T.J. Bandoz, Sulfur-doped carbon aerogel as a metal-free oxygen reduction catalyst, *ChemCatChem* 7 (2015) 2924–2931.
- [38] S.J. Clark, M.D. Segall, C.J. Pickard, P.J. Hasnip, M.J. Probert, K. Refson, M.C. Payne, First principles methods using CASTEP, *Z. Kristallogr.* 220 (2005) 567–570.
- [39] J.P. Perdew, K. Burke, M. Ernzerhof, Generalized gradient approximation made simple, *Phys. Rev. Lett.* 77 (1996) 3865–3868.
- [40] M. Endo, Y.A. Kim, T. Hayashi, T. Yanagisawa, H. Muramatsu, M. Ezaka, H. Terrones, M. Terrones, M.S. Dresselhaus, Microstructural changes induced in “stacked cup” carbon nanofibers by heat treatment, *Carbon* 41 (2003) 1941–1947.
- [41] J. Huang, D. Wang, H. Hou, T. You, Electrospun palladium nanoparticle-Loaded carbon nanofibers and their electrocatalytic activities towards hydrogen peroxide and NADH, *Adv. Funct. Mater.* 18 (2008) 441–448.
- [42] J. Ying, X.-Y. Yang, Z.-Y. Hu, S.-C. Mu, C. Janiak, W. Geng, M. Pan, X. Ke, G. Van Tendeloo, B.-L. Su, One particle@one cell: Highly monodispersed PtPd bimetallic nanoparticles for enhanced oxygen reduction reaction, *Nano Energy* 8 (2014) 214–222.
- [43] J. Ying, Z.Y. Hu, X.Y. Yang, H. Wei, Y.X. Xiao, C. Janiak, S.C. Mu, G. Tian, M. Pan, G. Van Tendeloo, B.L. Su, High viscosity to highly dispersed PtPd bimetallic nanocrystals for enhanced catalytic activity and stability, *Chem. Commun.* 52 (2016) 8219–8222.
- [44] W. Chen, J. Ji, X. Duan, G. Qian, P. Li, X. Zhou, D. Chen, W. Yuan, Unique reactivity in Pt/CNT catalyzed hydrolytic dehydrogenation of ammonia borane, *Chem. Commun.* 50 (2014) 2142–2144.
- [45] K. Li, Z. Jin, J. Ge, C. Liu, W. Xing, Platinum nanoparticles partially-embedded into carbon sphere surfaces: a low metal-loading anode catalyst with superior performance for direct methanol fuel cells, *J. Mater. Chem. A* 5 (2017) 19857–19865.
- [46] Y. Tao, W. Zhang, Li, D. Shang, Z. Xia, F. Wang, Fundamental principles that govern the copper doping behavior in complex clinker system, *J. Am. Ceram. Soc.* 101 (2017) 2527–2536.
- [47] Y. Tao, W. Zhang, D. Shang, Z. Xia, N. Li, W.-Y. Ching, F. Wang, S. Hu, Comprehending the occupying preference of manganese substitution in crystalline cement clinker phases: a theoretical study, *Cement Concrete Res.* 109 (2018) 19–29.
- [48] N.T. Cuong, D.H. Chi, Y.-T. Kim, T. Mitani, Structural and electronic properties of Ptn (n = 3, 7, 13) clusters on metallic single wall carbon nanotube, *Phys. Status Solidi B* 243 (2006) 3472–3475.
- [49] M. Shao, Q. Chang, J.-P. Dodelet, R. Chenitz, Recent advances in electrocatalysts for oxygen reduction reaction, *Chem. Rev.* 116 (2016) 3594–3657.
- [50] I.V. Zenyuk, S. Litster, Spatially resolved modeling of electric double layers and surface chemistry for the hydrogen oxidation reaction in water-filled platinum-carbon electrodes, *J. Phys. Chem. C* 116 (2012) 9862–9875.
- [51] G. Gupta, D.A. Slanac, P. Kumar, J.D. Wiggins-Camacho, J. Kim, R. Ryoo, K.J. Stevenson, K.P. Johnston, Highly stable Pt/ordered graphitic mesoporous carbon electrocatalysts for oxygen reduction, *J. Phys. Chem. C* 114 (2010) 10796–10805.
- [52] H. Wei, Z.-Y. Hu, Y.-X. Xiao, G. Tian, J. Ying, G. Van Tendeloo, C. Janiak, X.-Y. Yang, B.-L. Su, Control of the interfacial wettability to highly dispersed PtPd nanocrystals for efficient oxygen reduction reaction, *Chem. Asian J.* 13 (2018) 1119–11231.
- [53] W. Qian, R. Hao, J. Zhou, M. Eastman, B.A. Manhat, Q. Sun, A.M. Goforth, J. Jiao, Exfoliated graphene-supported Pt and Pt-based alloys as electrocatalysts for direct methanol fuel cells, *Carbon* 52 (2013) 595–604.
- [54] B. Lim, M. Jiang, P.H. Camargo, E.C. Cho, J. Tao, X. Lu, Y. Zhu, Y. Xia, Pd-Pt bimetallic nanodendrites with high activity for oxygen reduction, *Science* 324 (2009) 1302–1305.